Robust measurement of microbial reduction of graphene oxide nanoparticles using image analysis

Danielle T. Bennett, Anne S. Meyer#

Department of Biology, University of Rochester, Rochester, New York, United States

Running Head: Image Analysis of Microbial Graphene Oxide Reduction

Address correspondence to Anne S. Meyer, anne@annemeyerlab.org.

ABSTRACT

Shewanella oneidensis (*S. oneidensis*) has the capacity to reduce electron acceptors within a medium and is thus used frequently in microbial fuel generation, pollutant breakdown, and nanoparticle fabrication. Microbial fuel setups, however, often require costly or labour-intensive components, thus making optimization of their performance onerous. For rapid optimization of setup conditions, a model reduction assay can be employed to allow simultaneous, large-scale experiments at lower cost and effort. Since *S. oneidensis* uses different extracellular electron transfer pathways depending on the electron acceptor, it is essential to use a reduction assay that mirrors the pathways employed in the microbial fuel system. For microbial fuel setups that use nanoparticles to stimulate electron transfer, reduction of graphene oxide provides a more accurate model than other commonly used assays as it is a bulk material that forms flocculates in solutions with a large ionic component. However, graphene oxide flocculates can interfere with traditional absorbance-based measurement techniques. This study introduces a novel image analysis method for quantifying graphene oxide reduction, showing improved performance and statistical accuracy over traditional methods. A comparative analysis shows that the image analysis method produces smaller errors between replicates and reveals more statistically significant differences between samples than traditional plate reader measurements under conditions causing graphene oxide flocculation. Image analysis can also detect reduction activity at earlier time points due to its utilization of larger solution volumes, enhancing color detection. These improvements in accuracy make image analysis a promising method for optimizing microbial fuel cells that use nanoparticles or bulk substrates.

IMPORTANCE

Shewanella oneidensis (*S. oneidensis*) is widely used in reduction processes such as microbial fuel generation due to its capacity to reduce electron acceptors. Often, these setups are labor intensive to operate and require days to produce results, so use of a model assay would reduce the time and expense needed for optimization. Our research developed a novel digital analysis method for analysis of graphene oxide flocculates that may be utilized as a model assay for reduction platforms featuring nanoparticles. Use of this model reduction assay will enable rapid optimization and drive improvements in the microbial fuel generation sector.

INTRODUCTION

Shewanella oneidensis is a bacterium that can drive microbial fuel generation[1–5], breakdown of azo dye pollutants[6–8], and fabrication of nanoparticles[2] due to its capacity for transferring electrons to electron acceptors within a medium[2,7,9–11]. Natively, this electron transferral facilitates bacterial respiration using extracellular electron acceptors like Fe(III)[12]. Electron transfer by the *S. oneidensis* organism is accomplished through several alternative routes intercellularly and extracellularly, including electron shuttling by flavin secretion[13–16], through outer membrane extensions produced by the bacterium[10,17,18], or through direct membrane pathways[19,20]. Flavins are soluble shuttle molecules which are released by the bacteria into solution[21]. In both the nanowire and the direct membrane pathways, metal reduction has been largely attributed to a set of surface Mtr/Omc proteins[22,23] that includes three outer membrane decaheme c-type cytochromes (MtrC, MtrF, OmcA), two periplasmic decaheme cytochromes (MtrA and MtrD), and two outer membrane non-cytochrome proteins (MtrB, MtrE)[22–26]. These proteins funnel electrons to cytochromes embedded in the outer membrane of the bacterium, allowing extracellular electron transfer in particular for metallic iron electron acceptors[3,24,27]. This capacity also enables use of this organism to reduce a wide range of extracellular electron acceptors[11], including desalination of salt water[6–8,28] , bioremediation of pollutants in soil[28] and powering environmental sensors[4,29].

Since microbial fuel cell setups can be complex and require extended time periods to produce results[4,28], efficiency of the fuel cells may be improved using a model reduction assay to quickly test new reaction conditions. The reduction of the acceptor in microbial fuel cells may proceed through any of the *S. oneidensis* electron transfer pathways, and the specific reduction pathway that is utilized by the bacterium varies in different circumstances[16,30,31]. Flavin pathways seem to dominate in systems with insoluble electron acceptors and under certain ratios of electron donors and acceptors[16,30,31], nanowire pathways seem to dominate when the organism is under stress due to nutrient deficiency[3,10,18,32], and Mtr pathways are important in anaerobic conditions[33–35]. The dominant pathway can also depend on the type of electron acceptor present in the extracellular environment[21,36,37]. Thus, to improve the efficiency of microbial fuel-generating setups utilizing a model reduction assay, the model reduction assay must utilize the same reduction pathway as the fuel cell.

Model assays to monitor *S. oneidensis* reduction frequently involve observing the variation in absorbance over time as dye compounds such as methylene blue[13,38] or Congo red[13] are reduced and become colorless. Another common assay, the ferrozine assay, creates conditions of excess iron under which an iron transport pathway termed FoeE is particularly important in reduction[39]. The ferrozine assay is representative of reduction pathways involving soluble metal ions in solution or media with excess iron[39], while Congo red reduction features soluble electron acceptors, particularly those which utilize the Mtr pathway with dependence on the CymA cytochrome[13]. For insoluble electron acceptors such as nanoparticles or bulk conductive solids, these assays will not be appropriately representative. Plasmonic nanoparticles may also be used to monitor microbial electron transfer as observed by Graham et al. (2022)[40], and this approach offers direct insight into nanoparticle pathways and direct monitoring of electron transfer. However, this method is similar to electrochemical monitoring of microbial electron transfer in that it offers precise quantification of microbial electroactivity at small scale[41–44].

For rapid tuning of microbial fuel setups, which are usually performed at bulk scale, a graphene oxide reduction assay is advantageous as graphene oxide is inexpensive, scalable, and can be reduced rapidly[45]. Graphene oxide forms insoluble nanoparticle flocculates in solution with sizes ranging from 1 nm in diameter in colloidal solution to 20 μm in acidic or high-concentration conditions[46,47]. Graphene oxide reduction by *S. oneidensis* has been shown to require the Mtr respiratory pathway[15] with particular dependence on MtrF and CymA[48]. This reduction process is also enhanced by electron shuttling pathways, which are more prominent when the electron acceptor is a bulk substrate[15]. Graphene oxide reduction reactions can be performed under conditions that cause the graphene oxide to flocculate, a type of aggregation, which can take place in solution under certain pH and concentration conditions[46]. *S. oneidensis* reduction of graphene oxide flocculates may thus serve as a model assay for systems that reduce nanoparticles or bulk substrate. Graphene oxide flocculates form rapidly[46,49] and do not require the technical complexity of nanoparticle synthesis[23], making them well-suited for use as a model system of a microbial fuel cell that features nanoparticles. However, monitoring the absorbance of graphene oxide using traditional spectroscopic methods is challenging due to this flocculation, which causes increased error in readings due to drift of the large particles. Typically, assays are restricted to certain pH ranges and graphene oxide concentrations[45], or alternatively flocculates can be sonicated and filtered to remove them prior to analysis[11], both of which limit the use of these assays. Visually, reduction of graphene oxide produces a color change from light brown to dark black as the graphene oxide is reduced[23], and this visual color difference may be used to measure directly the transfer of electrons to bulk substrate or nanoparticle electron acceptors. Hence there is an opportunity for image analysis of graphene oxide reduction to provide quantitative information on the extent of reduction of the graphene oxide over time.

117 Image analysis methods are commonly used in nanoparticle sensing[50,51], in which images of
118 the samples are analyzed for the average 'color' of each. Color is interpreted using a set of
119 three vectors known as a 'color space'[52] such as RGB (red, green, and blue) which contains the
120 corresponding percentage of 'red', 'green,' or 'blue' for each pixel. For images that include
121 fluctuating lighting or reflections, the HSV color space (hue, saturation, and value) is more
122 robust due to the separation of lighting information into the saturation and value vectors[52–54].
123 By averaging the HSV vectors of a region of interest of an image of a graphene oxide sample
124 over time, the reduction of graphene oxide over time by *S. oneidensis* may be measured. This
125 method is advantageous for monitoring graphene oxide solutions that have flocculates present
126 because the averaging is performed over a larger area of the sample, thereby avoiding
127 confounding effects from the flocculates settling within the solution. This new method of
128 combining image analysis techniques with an unconventional graphene oxide reduction assay
129 will enable model assays for microbial fuel cells featuring bulk substrate and nanoparticles.

130 **RESULTS**

131 **Determination of the average Hue, Saturation and Value vectors for images of graphene**
132 **oxide.**

133 Custom Matlab™ code was written to determine the hue (H), saturation (S) and value (S) vector
134 distribution across images of graphene oxide solutions (Figure 1A). Images of experimental
135 samples were cropped to obtain a rectangular region of interest containing glare or reflection.
136 Points were then selected in regions with no glare or reflections (Figure 1B). Selection of 15
137 points or more was found to reduce the standard error of all selected points across each image
138 to 0.09 % or less of the vector value on average (Supplemental Figure 1). A 32 x 32 pixel box
139 was selected around each point (Figure 1C), and the average value of each pixel within the box

was calculated to obtain the average hue, saturation, and value vectors for each region of interest selected.

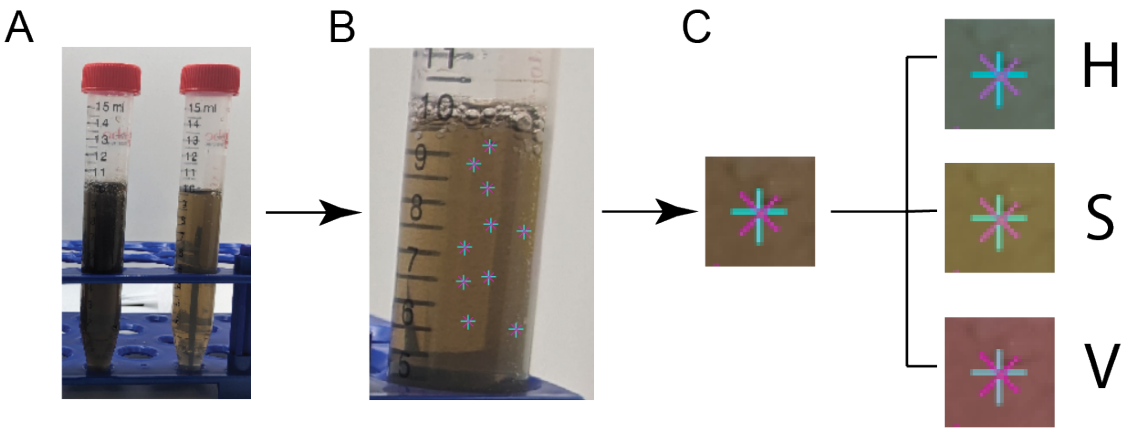

Figure 1: The workflow of the value vector analysis. A) A region of the image was selected that contains the least interference from the background of the sample. B) At least 12 points were selected that did not contain interference from tube labels or reflections. C) For each selected point, a 32 x 32 pixel box was cropped around the point, and the image information was separated into three vectors: hue (H), saturation (S) and value (V). The value vector contains information about the brightness or darkness of the image, represented as a number between 0 and 1, where 0 is the darkest and 1 is the lightest. The value vector was averaged over all the selected pixels to obtain an average value for each box. All boxes were then averaged to obtain an overall average value for each sample. This overall averaged value was used as a representation of the extent of graphene oxide reduction.

Correlation between average HSV value and graphene oxide concentration

To determine the suitability of image analysis for measuring graphene oxide reduction, experiments were performed to determine whether HSV value correlated with graphene oxide concentration. Different concentrations of graphene oxide were prepared, and image analysis values for the hue, saturation, and value vectors were measured (Figure 1).

The hue and saturation vectors did not vary linearly with increasing graphene oxide concentration, rather reaching a binary saturation point (Supplemental Figure 2). However, the value vector, which is representative of the brightness of an image[54], demonstrated linear

behaviour as a function of the graphene oxide concentration in some regions of the data (Figure 2). At lower concentrations of graphene oxide, increasing the graphene oxide concentration resulted in decreasing average HSV value of the samples. The average HSV value of the samples plateaued at graphene oxide concentrations around 40 %, or 0.40 g/L. Lower concentrations of graphene oxide between 6 – 12 % were used for future experiments in order to utilize a range over which the image analysis will be sensitive. These results demonstrated that the average HSV value measurement, as opposed to the hue or saturation, showed the closest correlation with increasing graphene oxide concentration and that this measurement approach could be a promising technique for monitoring graphene oxide reduction over time.

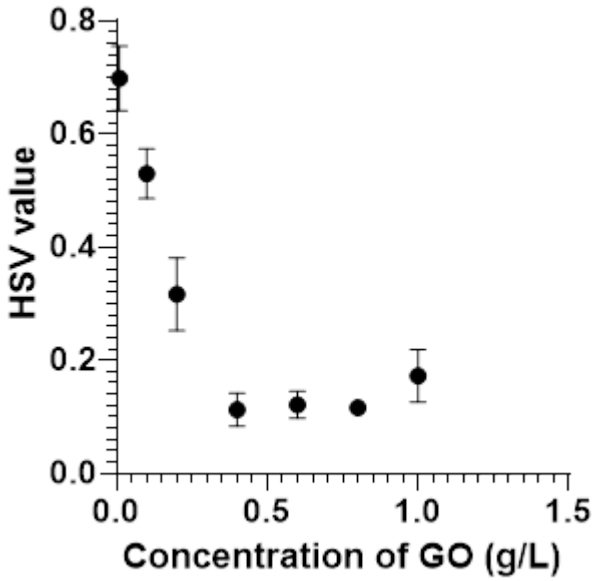

Figure 2: The average calculated HSV value vectors of samples with concentrations of graphene oxide varying from 0.01 – 1 g/L. Triplicate measurements were taken for each sample, and the results were averaged. The error was the standard deviation of these triplicate measurements.

Application of the image analysis methodology by naïve users

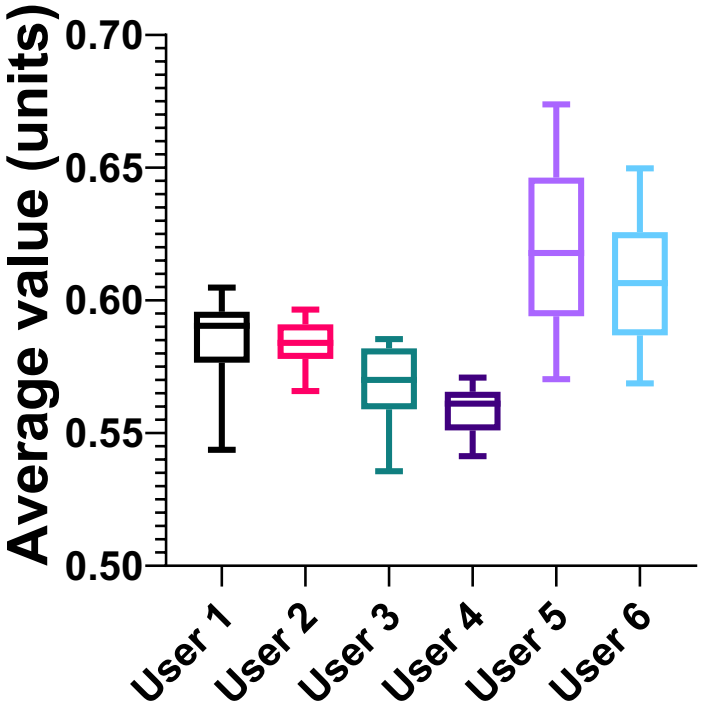

Figure 3: Image analysis measurements by six random users. Points were selected from the same image of three sample tubes at 3.5 hours of microbial graphene oxide reduction. The error bars represent the maximum and minimum values for each user, and the centre line represents the median. The boxes extend from the 25th -75th percentiles.

In order to observe the user-friendliness of the image analysis technique, an experiment was performed to determine the consistency of user-selected HSV values without prior instruction. Users with no prior experience with the image analysis technique were asked to select ten or more points that accurately represented the color of an image of microbial graphene oxide reactions in 40-mL sample tubes at the 3.5-hour timepoint (Figure 3). User selections produced HSV values that were significantly statistically different, with a one-way ANOVA test resulting in a p-value of < 0.0001 (6.053, 5). Individual results for unpaired t-test p-values are presented in SI Table 1. Groups 1 and 2, 3 and 4, and 5 and 6 were not statistically different from each other but were statistically different from each other group. The average of all user-selected HSV values, considered across all users, was 0.586 ± 0.007 units, where the error represents the standard deviation of all points. This error represents

191 1.2% of the overall average HSV value. Hence, although different users selected statistically
192 different values from the same sample (Supplemental Figure 3), due to the consistency of the
193 HSV value vector across a sample the error from this variance was minimal.

194 **Image analysis provides more sensitive measurements of graphene oxide reduction by *S.***
195 ***oneidensis* than plate reader absorbance measurements**

196 Since plate reader absorbance measurements are the current standard for measuring bacterial
197 graphene oxide reduction, experiments were performed to compare the accuracy and sensitivity
198 of the image analysis method with plate reader absorbance measurements. A solution of
199 graphene oxide was reduced by *S. oneidensis* bacteria either with or without lactic acid as an
200 electron donor. For this experiment, aliquots were taken from each sample at specific time
201 points and used for plate reader analysis (Figure 4A, Supplemental Figure 4) as well as imaging
202 the samples, allowing for the two analysis techniques to be directly compared (Figure 4B). The

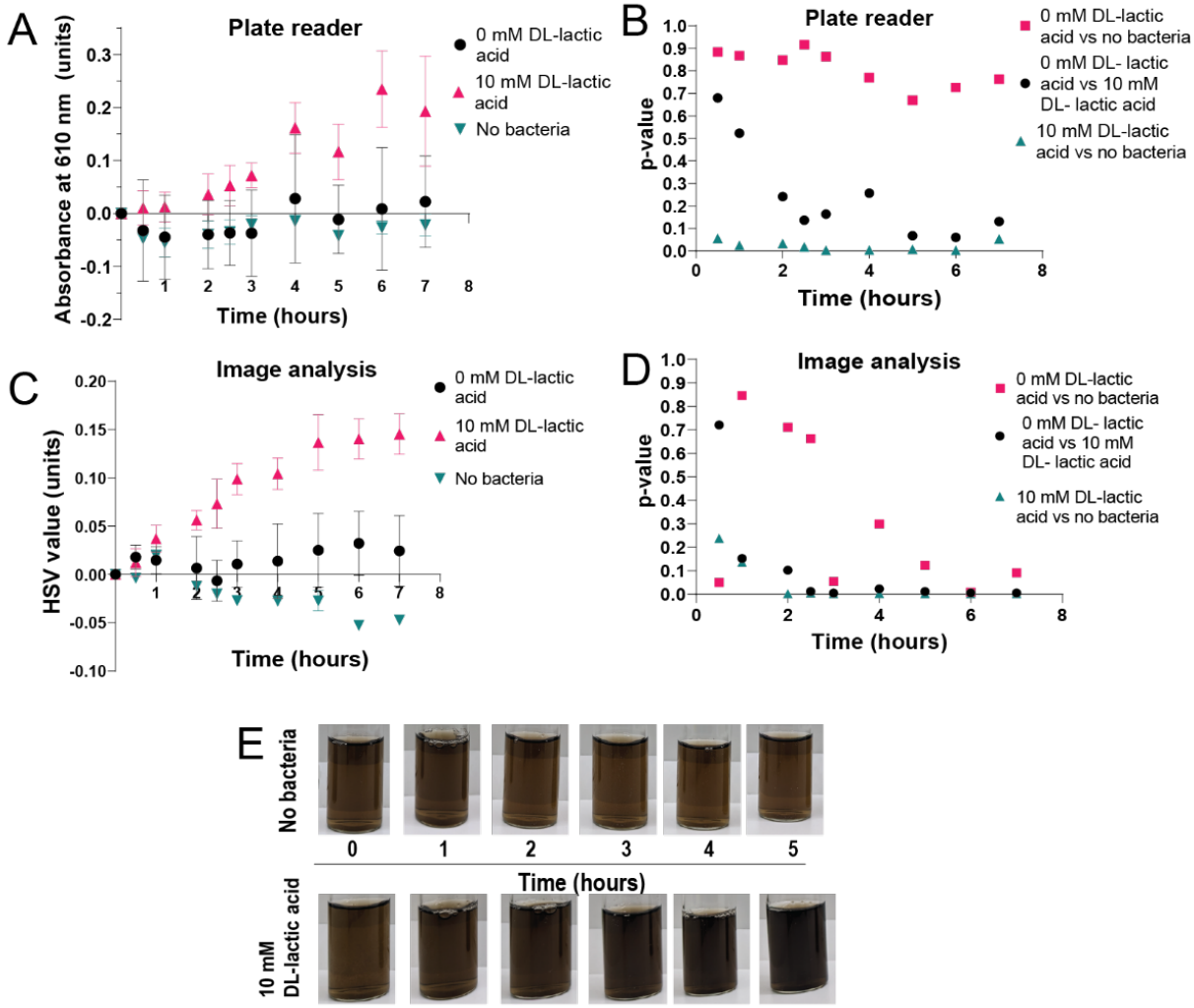

Figure 4: Comparison of plate reader and image analysis of bacterial graphene oxide reduction. A) Analysis of the reduction of graphene oxide by *S. oneidensis* over time by plate reader measurements of the absorbance of a 100 µL aliquot at 610 nm. The statistical difference between samples was calculated to have a p value = 0.0007, with an W ratio of 9.046 (3.000, 17.71). B) Bootstrapping statistical analysis of the p-value of different sample comparisons for the plate reader data at different timepoints. C) Image analysis measurements of the same samples, resulting in an averaged HSV value representation of the graphene oxide reduction. The statistical significance of the difference between samples was calculated to have a p-value < 0.0001 with an W ratio of 20.06 (3.000, 17.67). The errors represent the standard deviation of triplicate repeats of each sample. D) Bootstrapping statistical analysis of the p-value of different sample comparisons for the image analysis data at different timepoints. E) Images of a single sample of graphene oxide with no bacteria (top) or 10 mM lactic acid as an electron source (bottom) over time. Samples with no bacteria were used as a control to detect background levels of graphene oxide reduction. The samples with 0 mM lactic acid and with 10 mM lactic acid both contained identical initial concentrations of bacteria. The statistical significance of the difference between samples was calculated using one way ANOVA with a Welch's correction as well as bootstrapping analysis.

lack of electron donor present in the samples with 0 mM lactic acid was expected to result in

204 minimal bacterial reduction rates, and thus determining the level of difference between samples
205 with and without lactic acid will allow for comparing the sensitivity of each analysis technique.
206 For these results, initial measurements were subtracted from subsequent measurements to
207 normalize for variation in graphene oxide amounts between samples and allow for comparison
208 between two techniques with different y-axis units. Any negative values for the samples were
209 assumed to be due to random fluctuation of the measurement paired with this subtraction. Plate
210 reader absorbance measurements of timed aliquot extractions were taken at 610 nm in a 96 well
211 plate, and at this same time-point the samples were imaged to provide a direct comparison with
212 the image analysis.

213 The plate reader measurements showed an increase in average absorption over time after an
214 initial lag phase for the samples containing lactic acid, indicating reduction of the graphene
215 oxide (Figure 4A). Minimal changes in absorption were measured for the samples without
216 lactic acid or without bacteria. The image analysis results also showed an increase in average
217 HSV value over time for the samples containing lactic acid, though the apparent lag phase was
218 shorter (Figure 4C). The no-lactic-acid and no-bacteria control samples again showed minimal
219 changes in absorption. The limit of detection of a sensing assay may be estimated by obtaining
220 the overall mean of a control sample and then adding three standard deviations to obtain an
221 upward estimate[55,56]. To compare the different techniques, this limit of detection was
222 normalised by the highest detected value of the assay. Since samples often had slightly different
223 starting absorbances, the initial absorbance for an individual sample was subtracted from all
224 subsequent values to normalize the data so that samples could be compared. The normalised
225 value was 0.07 units for the plate reader and 0.29 units for the image analysis. This result shows
226 that the limit of detection of the plate reader assay was lower than that of the image analysis
227 and thus the plate reader is more sensitive. However, the lower W ratio (analogous to the F
228 statistic[57]) for the plate reader analysis measurements indicates that the statistical difference

229 between the samples with 10 mM lactic acid, without lactic acid, and without bacteria is lower
230 for the plate reader measurements than for the image analysis data[57]. This result indicates that
231 there is improved statistical separation between different sample types for the image analysis
232 data.

233 To further investigate the statistical differences between sample types, bootstrapping analysis
234 was performed on both datasets to provide an improved p-value analysis for small datasets at
235 different time points[58]. For the plate reader analysis method (Figure 4B), the p-value did not
236 reach a confidence interval of 95 % for the comparison of the sample with 0 mM lactic acid
237 and the sample with no bacteria, so these groups were not significantly different. The
238 comparison between the plate reader samples with 0 mM lactic acid and 10 mM lactic acid
239 revealed that a 95 % confidence interval was reached after 5 hours. This result indicates that
240 these groups became statistically significantly different at the 5-hour timepoint. The plate
241 reader sample containing 10 mM lactic acid and the sample with no bacteria were
242 significantly statistically different throughout the experiment. In contrast, bootstrapping
243 analysis of the image analysis method (Figure 4D) indicated that the sample with 0 mM lactic
244 acid and the sample with no bacteria reached statistically significant separation after 6 hours,
245 and the 0 mM lactic acid sample and the 10 mM lactic acid sample reached statistically
246 significant separation earlier at 2.25 hours. The sample with 10 mM lactic acid and the
247 control sample with no bacteria became significantly statistically different at 2 hours. Since
248 the three groups were expected to have a large difference in the rate of extracellular reduction
249 for graphene oxide, reaching significant statistical separation at earlier timepoints indicates
250 improved precision of the image analysis technique.

251 Visual comparison of the vials of two different samples over time, with one containing no
252 bacteria and one with 10 mM lactic acid added as an electron donor, showed a qualitative
253 difference at the two-hour time point, with the 10 mM lactic acid sample appearing darker

254 (Figure 4E). This difference was reflected in the image analysis data but not the plate reader
255 measurements. Reduction was indicated by the separation between the control and samples
256 with lactic acid. The image analysis data trendline (Figure 4C) also plateaus around the five-
257 hour time point, whereas the plate reader data does not show a clear plateau (Figure 4A). For
258 bacterial reduction, a Gompertz trendline exhibiting a lag period, a period of exponential
259 growth and then a plateau is expected[59,60]. This fit is often used for bacterial growth curve
260 fitting[59,61] and is applicable for bacterial consumption of analytes[59]. The plateau in the image
261 analysis data trendline (Figure 4C) could indicate expected Gompertz reduction activity, or it
262 could indicate that the sensor was saturated. The clear plateau for the image analysis method
263 that is not present for the plate reader analysis method is indicative of the higher precision of
264 the image analysis technique.

265 **Influence of differing initial bacterial densities on measurements of graphene oxide**
266 **reduction by *S. oneidensis***

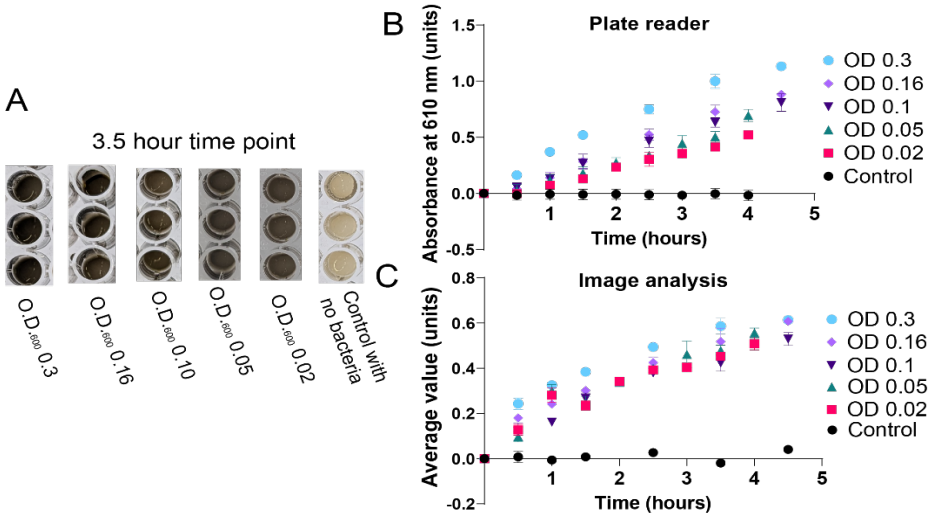

Figure 5: Comparison of plate reader and image analysis of bacterial graphene oxide reduction for differing initial bacterial densities. A) An example image of microplate wells containing graphene oxide solutions with different initial $O.D._{600}$ concentrations of *S. oneidensis* at the 3.5-hour timepoint. B) Plate reader and C) image analysis measurements of these samples over time. Each sample was measured in triplicate, and the errors are representative of the standard deviation of these triplicate measurements. Some errors were too small to visualize on the graph. The control samples contained no bacteria. The statistical significance of the difference between sample sets was calculated using one way ANOVA. For comparison of samples with the control sample, the F statistic for the plate reader data was 5.158 (5, 42) with a p value = 0.0009. The F statistic for the image analysis data was 2.131 (5,40), with a p value = 0.0814.

Since bacterial cells[62] and reduced graphene oxide[63] can have overlapping optical density absorbance peaks, techniques to measure graphene oxide reduction can potentially be confounded by the density of bacteria cells in the samples. Experiments were thus performed to examine the impact of differing initial $O.D._{600}$ densities of bacteria on both the plate reader and image analysis techniques for measuring bacteria graphene oxide reduction. To avoid a plateau from analyte consumption and improve bacterial growth, electron donors were provided in excess via lysogeny broth. Providing too much excess lactic acid in combination with the high ion concentrations of the Minimal media causes near-instantaneous flocculation of graphene oxide into large flakes that settle too fast for imaging[46]. To circumvent this issue, lysogeny broth was used to provide electron donors. *S. oneidensis* bacteria were added at initial $O.D._{600}$ densities ranging from 0.02 to 0.3. Timepoint aliquots were analysed by the plate reader

279 and image analysis for direct comparison (Figure 5, Supplemental Figure 5) as outlined
280 previously.

281 Observation of the samples at a timepoint of 3.5 hours (Figure 5A) demonstrated dramatic
282 differences between the control sample and the bacteria-containing samples, which were much
283 darker in appearance. A one-way ANOVA analysis of the plate reader measurement data
284 (Figure 5B) resulted in a p-value of 0.0009 (5.158, 5), showing significant statistical differences
285 between groups, while the image analysis data (Figure 5C) resulted in a p-value of 0.0814
286 (2.131,5), showing non-significant statistical differences between groups overall. A full
287 comparison of unpaired t-test p-values for the plate reader analysis and the image analysis may
288 be found in SI Tables 2-3. Comparison of individual unpaired t-test p-values revealed that both
289 analysis methods had statistically significant differences between the control sample and the
290 samples with bacteria. For example, the p-value of the $O.D._{600}$ 0.3 sample compared to the
291 control sample without bacteria was 0.0011 (4.112,14) for the plate reader analysis and 0.0007
292 (4.543,12) for the image analysis. Non-significant differences were observed between other
293 samples for both analysis techniques, with p-values for the image analysis being predominantly
294 higher on average. The exception was for the comparison between the $O.D._{600}$ 0.3 sample and
295 the $O.D._{600}$ 0.02 samples, which resulted in a significant difference for the plate reader analysis,
296 with a p-value of 0.0493 (2.153,14), and a non-significant difference for the image analysis,
297 with a p-value of 0.4491 (0.7787,14). The plate reader measurement data (Figure 5B) showed
298 linear trendlines for the samples containing bacteria whereas the image analysis data for the
299 samples containing bacteria (Figure 5C) had a slight plateau. The increased difference between
300 samples containing varying starting bacterial densities seen for the plate reader analysis may
301 likely be attributed to differences in the background scattering of the bacteria, which increases
302 with increasing $O.D._{600}$ instead of increased reduction activity.

303 **Image analysis measurements are more accurate than plate reader measurements of**

304 **graphene oxide reduction by *S. oneidensis* electroactivity-deficient strains**

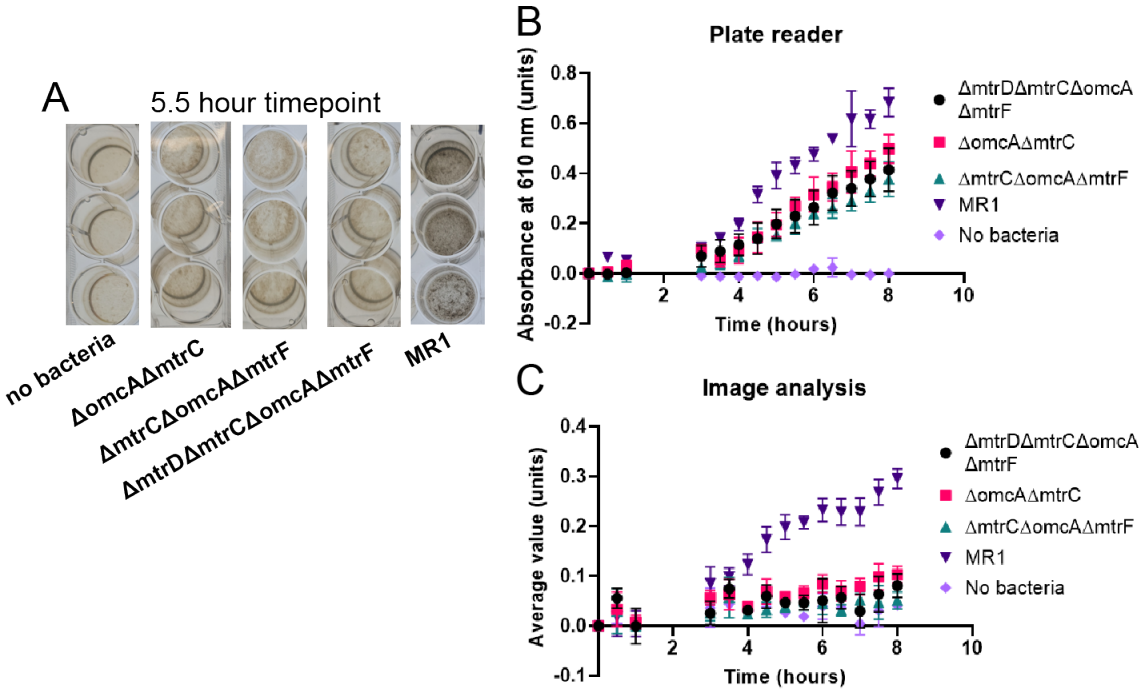

305

306 Figure 6: Comparison of plate reader and image analysis measurements on the electroactivity
307 of *S. oneidensis* electroactivity-deficient strains. A) Image of plate reader wells at the 5.5-hour
308 timepoint for graphene oxide reduction reactions containing no bacteria, *S. oneidensis*
309 knockout strains *(ΔomcAΔmtrC, ΔmtrCΔomcAΔmtrF,* or *ΔmtrDΔmtrCΔomcAΔmtrF)*, or wild-
310 type *S. oneidensis* MR-1. B) Plate reader analysis results for three replicate samples of each
311 strain. C) Image analysis results for six replicate samples of each strain. Errors are standard
312 deviations of replicate samples.

313

314 To determine whether the image analysis technique could be applied to *S. oneidensis* strains

315 with varying electroactivity abilities, image analysis and plate reader analysis observations

316 were performed for the microbial reduction of graphene oxide by electroactivity-deficient *S.*

317 *oneidensis* knockout strains compared to the wild-type MR-1 strain. The knockout strains

318 were deleted for genes affecting outer membrane chromophores (*ΔmtrDΔmtrCΔomcAΔmtrF,*

319 *ΔomcAΔmtrC,* and *ΔmtrCΔomcAΔmtrF*). Since these chromophores are responsible for

320 transmission of extracellular electrons, the electroactivity of these strains is expected to be

321 reduced[19,64–66]. At intermediate timepoints during the reduction reactions, large differences

322 were observed visually between the reduction level of MR-1, which showed dark coloration
323 indicative of extensive graphene oxide reduction, and the three knockout strains and the
324 control sample containing no bacteria, which were much lighter in color (Figure 6A,
325 Supplemental Figure 6). Comparison of the electroactivity of the *ΔmtrDΔmtrCΔomcAΔmtrF*
326 strain with four electroactivity genes knocked out and the *ΔmtrCΔomcAΔmtrF* strain with
327 three genes knocked out using an unpaired t-test produced a p-value of 0.6922 (0.4404, 26)
328 for the plate reader analysis (Figure 6B) and 0.1712 (1.407, 26) for the image analysis (Figure
329 6C), indicating that there is not significant difference in electroactivity between the two
330 strains. Statistical comparison of the results for the triple knockout *ΔmtrCΔomcAΔmtrF* strain
331 versus the double knockout *ΔomcAΔmtrC* strain revealed a p-value of 0.3478 (0.9563, 26) for
332 the plate reader analysis (Figure 6B) and 0.0160 (2.573, 26) for the image analysis (Figure
333 6C), indicating that only the image analysis detected a significant difference between the two
334 strains. Comparison between the MR-1 wild-type strain and the quadruple knockout
335 *ΔmtrDΔmtrCΔomcAΔmtrF* strain indicated a p-value of 0.0568 (1.994, 26) for the plate
336 reader analysis (Figure 6B) and 0.0004 (4.024,26) for the image analysis (Figure 6C). The
337 dramatic visual differences between the wild-type and knockout strains are in agreement with
338 the image analysis results, and also align with previous observations of major differences in
339 electroactivity between the strains[19,64–66], indicating that the image analysis measurements are
340 a more accurate representation of the reduction reaction in these electroactivity-deficient
341 strains.

342 **Image analysis of scaled-up graphene oxide reduction reactions**

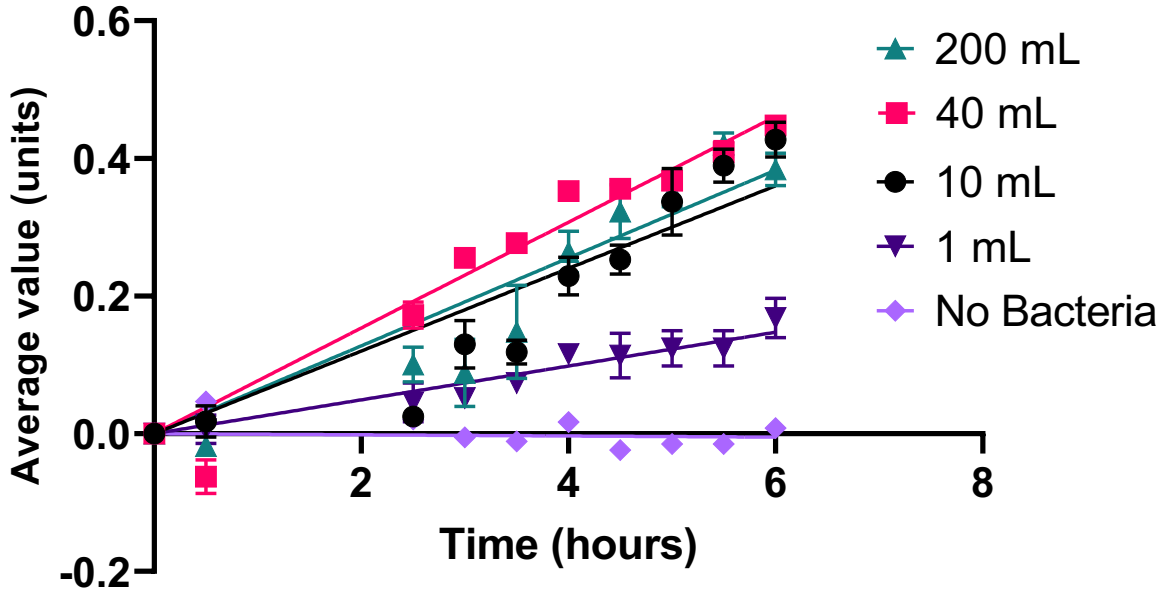

Figure 7: Image analysis measurements of bacterial graphene oxide reduction reactions performed with differing reaction volumes. Microbial graphene oxide reduction was performed in different volumes (200 mL, 40 mL, 10 mL, 1 mL) and monitored over time using image analysis. A control sample of 1 mL with no bacteria was included as a control. Errors are the standard deviation of three samples for each point. Linear regressions with 95 % confidence are included; regression lines pass through the origin.

To determine the impact of reaction scale on image analysis of microbial graphene oxide reduction, image analyses were performed on reactions with volumes ranging from 1 mL to 200 mL. Comparison between reactions of different volumes indicated a measurable impact of the scale of the reaction on the reduction rate (Figure 7). The 1-mL samples showed the slowest reduction over time, with a rate of 0.024 ± 0.001 units per hour. Interestingly, the 10-mL and 200-mL samples performed similarly over time, with reduction rates of 0.060 ± 0.003 units per hour and 0.063 ± 0.003 units per hour respectively. An unpaired t-test of the two samples produced a p-value of 0.8529 (0.1881, 18), indicating no significant difference. While the 40-mL sample had the highest reduction rate of 0.077 ± 0.002 units per hour, an unpaired t-test comparison between the 40-mL and the 200-mL sample produced a p-value of 0.5005, indicating no significant difference between the two groups. The higher reduction

362 rate observed for the 40-mL samples may therefore be attributable to variable lag phases of
363 the microbial reduction reaction among the different-volume samples. Overall, the image
364 analysis technique was able to measure progressive microbial graphene oxide reduction over
365 time for samples varying 200-fold in reaction volume.

366

367 **DISCUSSION**

368 Graphene oxide reduction assays are promising candidates for application as a model assay for
369 *S. oneidensis* reduction platforms featuring nanoparticles, since the flocculates formed by the
370 graphene oxide would imitate nanoparticle electron acceptors[15,23]. Such a model assay would
371 enable quick optimization of the microbial reduction platform with less resource expense.
372 However, tailoring the electron receiver to match the original platform is important since *S.*
373 *oneidensis* has multiple reduction pathways, and the dominant pathway is influenced by media
374 composition[30] or the specific electron acceptor[6,19,30,67]. Graphene oxide is well-suited for this
375 purpose, but measuring the progression of the reduction reaction accurately via absorbance
376 assays is difficult due to the flocculates. In this study, we compared traditional absorbance
377 measurements utilizing a microwell plate reader as the gold standard[68] with a novel digital
378 image analysis method for a *S. oneidensis* extracellular reduction assay featuring graphene
379 oxide flocculates[23]. The digital analysis was first optimized by determining which vector from
380 the HSV color space would correlate most closely with graphene oxide concentration, guided
381 by the hypothesis that correlation between an HSV vector and the graphene oxide concentration
382 increase, which also causes similar darkening of the sample, would be representative of the
383 color change caused by graphene oxide reduction. The HSV value vector varied linearly with
384 increased graphene oxide within a defined range of concentrations (Figure 2), unlike the hue
385 and saturation vectors (SI Figure 1). Hue has a sharp cut off when the colour was majority
386 black and is thus unsuitable for monitoring gradual changes over time. Saturation was

387 seemingly uncorrelated with the concentration of graphene oxide and was thus unsuitable. The
388 value vector decreases with increasing graphene oxide concentration and plateaus, making it
389 the best candidate for monitoring graphene oxide concentration using image analysis. From
390 this data, it was hypothesized that the HSV value vector could be utilized via image analysis to
391 be representative of graphene oxide reduction within a solution due to bacterial reduction,
392 producing measurements varying from 0 (lightest) to 1 (darkest). A comparison of points
393 selected by random users with no prior experience with the image analysis technique
394 demonstrated that the HSV values of the points had an overall standard deviation between 6
395 different users of 1.2 % (Figure 3). This result illustrates that the image analysis technique
396 produces consistent, reproducible results with minimal training required.

397 The image analysis technique was then used to measure a samples in a bacterial graphene oxide
398 reduction assay, and these data were compared to measurements taken by a plate reader,
399 currently the most standard method for quantifying bacterial reduction assays[68]. Analysis
400 measurements were compared for samples containing differential levels of lactic acid as an
401 electron donor for the *S. oneidensis.* The guiding hypothesis of this experimental set was that
402 the samples with no electron donor would have slow extracellular reduction compared to those
403 with electron donor present[23,69,70] since *S. oneidensis* consumes lactic acid as an electron donor
404 and transfers the electrons extracellularly to the graphene oxide flocculates[30,37,71]. *S. oneidensis*
405 will eventually use the acetate it produces as a waste product as an electron source, but this
406 reaction proceeds relatively slowly[14,72]. Thus, the statistical differences between samples would
407 provide a measurement of the sensitivity and accuracy of the analysis method. The graphene
408 oxide in the control solutions with no bacteria became lighter over time (Figure 4), which could
409 be due to some larger flocculates being degraded by the shaking conditions of the experiment[73].

410 Image analysis measurements (Figure 4A) showed larger differences between experimental
411 and control samples and smaller error bars when compared to the plate reader measurements

412 for these bacterial graphene oxide reduction experiments (Figure 4B). This increased error was
413 likely due to two main challenges with absorbance measurements of the graphene oxide assay.
414 Firstly, graphene oxide can form nanoparticle-like flocculates, particularly under acidic
415 conditions[46] and can be formed into small nanoparticles by *S. oneidensis*[23]. These flocculates
416 settle to the bottom of the 96 microwell plate over time, which will affect the reading taken by
417 the plate reader by variably obstructing the light source. The image analysis method can select
418 small sections of the flakes themselves and analyse the color, and hence is not dependent on
419 light translation through a sample. Secondly, graphene oxide absorption is usually monitored
420 by observing the shift in the absorbance maximum from 226 nm to 262 nm for reduced
421 graphene oxide[63]. However, due to the presence of UV-active components in the minimal
422 media and the bacteria themselves, the intensity of this peak will be obfuscated by the other
423 components of the media. Instead, a broad absorbance peak centred around 610 nm can be used
424 for monitoring the reduction of graphene oxide[45]. Graphene oxide has a major absorption peak
425 centred at 250 nm with a secondary broad peak at 450 nm[74]. As graphene oxide is reduced, the
426 absorbance maximum becomes red-shifted, with an increase in absorbance in higher
427 wavelengths[75]. The 610 nm absorption peak of the reduced graphene oxide overlaps with the
428 absorption of the bacteria, usually measured at 600 nm[76]. *S. oneidensis* absorbs from 350 nm
429 to 650 nm, exhibiting peaks at 370 nm, 540 nm and 550 nm [77,78] with the absorbance gradually
430 decreasing as wavelength increases. Thus, monitoring the absorbance of GO solutions at 610
431 nm can detect the appearance of reduced GO without crossover with the bulk of the bacterial
432 absorption signal. However, some interference from the bacterial scattering is unavoidable.
433 Cheng et al. (2014)[79] found similar interference for their electrochromic assay, which required
434 careful monitoring of bacterial densities as analysis progressed. The image analysis does not
435 encounter this challenge as it is not measuring absorption of a wavelength value but visual
436 color change. This independence ensures that variations in bacterial growth do not interfere

437 with the accuracy of measurements, which is crucial for maintaining consistency in data
438 analysed between samples. The larger area of analysis employed for the image analysis method
439 also reduces the impact of the flocculates. The image analysis measurements showed increased
440 statistically significant differences between different sample types, less overlap of error bars,
441 and the trendline contained a lag phase and a plateau consistent with the Gompertz growth
442 expected from microbial reduction[59] compared to the corresponding the plate reader
443 measurements (Figure 3B). As the three samples groups are expected to have a large difference
444 in the extracellular reduction of graphene oxide, this improved separation suggests improved
445 sensitivity of the image analysis technique.

446 A plateau in graphene oxide reduction was expected to be observed at later time points of the
447 bacteria reduction assays when the bacteria have reached high cell densities or consumed all
448 lactate present within the sample[80]. Consumption of lactate by *S. oneidensis* has been reported
449 at a rate of 11.8 mM/hour at high concentration of bacteria ($O.D._{600} \sim 0.2$)[70]. The plateau
450 observed by the image analysis at the five-hour time point for reduction samples containing 10
451 mM of lactic acid was therefore expected (Figure 3A). However, the plateau could also be due
452 to earlier saturation of the image analysis measurement due to larger volumes of analysis. This
453 is unlikely as further experiments obtained a Value vector maximum of 0.55 units, compared
454 to the plateau maximum of 0.15 units from this experiment. The lack of plateau for the plate
455 reader measurements could be due to decreased resolution of the method or increased range of
456 measurement. Overall, the image analysis data offered high resolution compared to the greater
457 sensitivity of the plate reader analysis method. As *S. oneidensis* is frequently used for
458 bioreactor research, information on the rate of reduction over time is important for improving
459 the efficiency of such systems[69,71] so higher resolution resulting in earlier detection of reduction
460 using the digital analysis is advantageous.

461 To further test the impact of bacteria concentration on graphene oxide measurements, samples
462 containing bacteria at different initial $O.D._{600}$ concentrations were investigated. This
463 experiment was designed to determine whether the overlapping optical density absorbance
464 peak of the bacteria with that of the graphene oxide would cause erroneous measurements of
465 graphene oxide reduction in conditions with higher bacterial density. To aid the bacterial
466 growth in this experiment, electron donors and nutrients were provided in excess. Both the
467 plate reader analysis and image analysis showed statistically significant differences between
468 control samples with no bacteria and samples with bacteria. These differences resulted in
469 higher statistical difference for the image analysis. However, overall analysis of the different
470 methods using one way ANOVA revealed larger statistical differences between groups of the
471 plate reader analysis. Increased reduction rates with increased concentration of bacteria were
472 not necessarily expected[81] as *S. oneidensis* slows its electron transfer during log phase growth[82].
473 The differences seen for the plate reader samples, particularly those with the highest initial
474 $O.D_{600}$, were then likely caused by interference from the spectral overlap between the bacterial
475 absorbance and the reduced graphene oxide absorbance measurement at 600 nm. The lack of
476 this effect in the image analysis measurements demonstrates its effectiveness of the image
477 analysis technique in a range of different experimental conditions, overcoming challenges
478 presented in the absorbance measurements of graphene oxide reduction assays.

479 The increased accuracy of the image analysis method over plate reader measurements was also
480 observed for reactions of graphene oxide reduction by different strains of *S. oneidensis*
481 featuring deleted electroactivity genes (Figure 6). Larger numbers of samples could be analysed
482 for the image analysis technique since the plate reader is only able to monitor one 24-well
483 microplate at a time, but there is no such restriction for image analysis. Knockout strains
484 affecting the extracellular electron transport genes *ΔmtrDΔmtrCΔomcAΔmtrF* and
485 *ΔmtrCΔomcAΔmtrF* were revealed by unpaired t-tests to have statistically indistinguishable

486 reduction activity for both analysis methods. However, comparison of *ΔomcAΔmtrC* and
487 *ΔmtrCΔomcAΔmtrF* resulted in statistically significant differences only for the image analysis
488 method and not for the plate reader analysis, as was also observed upon comparison between
489 the MR1 wild-type strain and the *ΔmtrDΔmtrCΔomcAΔmtrF* quadruple knockout strain (Figure
490 6). Significant differences in graphene oxide reduction are expected between the wild-type
491 strain and knockout strains wherein members of the extracellular electron transport pathways
492 are deleted. For example, reduction of electroactivity in a *cymA* knockout strain of 80% was
493 observed in comparison to the wild type[7], and similar extreme reduction in electroactivity is
494 consistently observed across literature[67,70,83,84]. The *ΔmtrFΔomcA* and *ΔomcAΔmtrF* strains of
495 *S. oneidensis* were observed to reduce iron oxide at only 5 % the rate of the wild-type strain[93].
496 The larger differences between wild-type and knockout strains observed by the image analysis
497 when compared to the plate reader analysis demonstrates the higher accuracy of the image
498 analysis technique as well as its applicability to a range of microbial strains with varying
499 electroactivity.

500 Another advantage of the image analysis technique when compared to plate reader analysis is
501 that far larger solution volumes may be analysed with the image analysis. Microbial reactors
502 are generally operated at scales of several hundred millilitres[76,85–88], and scale can have a
503 notable impact on catalytic reactions[89,90]. It is thus important to investigate the impact of scale
504 upon catalytic reactions, and the use of graphene oxide reduction as a model may enable this
505 without testing expensive catalytic components. Comparison of the microbial reduction of
506 graphene oxide at different scales (Figure 7) demonstrates surprising results at scale. While the
507 1-mL samples demonstrated the slowest microbial reduction rates, the 10-mL, 40-mL, and 200-
508 mL samples demonstrated higher reduction rates and were not significantly different from each
509 other. These analyses indicated that the image analysis method was able to measure microbial
510 graphene oxide reduction rates in a range of reaction volumes varying by 200-fold. The

differences observed in reduction rates could derive from multiple factors that affect microbial processes at scale[91,92]. Mixing times can increase when the reaction vessel becomes larger, creating negative impacts on microbial performance due to gradients in nutrients or temperature[91]. Broth hydrostatic pressure, which rises as solution volume increases, may also disrupt microbial processes due to elevated gas partial pressure[91]. As these processes have many confounding factors, direct testing through scalable approaches such as the image analysis technique is crucial to determine the appropriateness for industrial applications[92]. Image analysis techniques are also advantageous for industrial applications due to their ease of use[79] and the relative low cost of the technique. The smartphone used within this work cost $230 USD, in comparison to the plate reader used which cost $35,999 USD.

This work compares image analysis of bacterial graphene oxide reduction with more traditional absorption measurement collection with a microplate reader. The digital image analysis avoids increased variance from graphene oxide flocculate settling and overlap between the bacteria and the graphene oxide absorbance spectra. These features result in increased resolution of the digital image analysis, enabling earlier detection of reduction activity as well as increased statistically significant differences between different sample types. This new method creates the opportunity for a model assay for *S. oneidensis* reduction reactions that emulates interactions between the organism and nanoparticles or bulk conductive substrates. The application of this technique as a model assay could improve the speed of microbial fuel cell optimization for fuel cells containing bulk substrates or nanoparticles, accelerating the rate of advancement in this field.

EXPERIMENTAL METHODS

Bacterial strains and culturing

534 The bacterial cultures used in this work include *S. oneidensis MR-1* (ATCC® 700550™); *S.*
535 *oneidensis ΔomcAΔmtrC* (JG749, Coursolle and Gralnick (2010)[93]); *S. oneidensis*
536 *ΔmtrDΔmtrCΔomcAΔmtrF* (JG1101, Coursolle and Gralnick (2010)[93]); and *S. oneidensis*
537 *ΔmtrCΔomcAΔmtrF* (JG596, Coursolle and Gralnick (2010)[93]). *S. oneidensis* cultures were
538 grown from freezer stocks stored in 25% glycerol at -80 ºC. Lysogeny broth (LB) media was
539 prepared by dissolving tryptone (0.14 M, Sigma-Aldrich), yeast extract (15 mM, Sigma-
540 Aldrich) and NaCl (0.17 M, Sigma-Aldrich) in de-ionised water. This solution was autoclaved
541 for 30 minutes on a fluid cycle at 121 ºC and stored at room temperature. Frozen bacterial
542 cultures were streaked onto LB-agar plates and incubated at 30 ºC overnight. The following
543 day, a single colony was isolated and grown in LB (5 mL) at 30 ºC overnight under continuous
544 shaking (200 rpm). These overnight cultures were used for graphene oxide reduction
545 experiments.

546 **Graphene oxide reduction assay**

547 A solution of Minimal media was prepared as in Edwards, Jelusic, Kosko, McClelland,
548 Ngarnim, Chiang, Lampa-Pastirk, Krauss, and Bren (2023)[94]; details are presented in SI Tables
549 4-7. To this solution, graphene oxide (0.12 g / L) was added. This solution was divided into 20
550 mL aliquots in individual 40 mL Environmental Protection Agency (EPA) vials (Sigma-
551 Aldrich 23188). DL-lactic acid (10 mM, lactic acid) was added to some samples as an electron
552 donor[37]. All samples were adjusted to pH 7 with 10 M sodium hydroxide. Nitrogen gas was
553 bubbled though each vial for 10 minutes to create anaerobic conditions, which promotes
554 increased lactate consumption by the *S. oneidensis*[30]. Overnight cultures of *S. oneidensis*
555 prepared as described above were added to each vial at a 1:100 dilution, with three vials lacking
556 bacteria to serve as a negative control. The samples were incubated at 30 ºC under continuous
557 shaking (200 rpm).

558 **Graphene oxide reduction assay comparing different bacteria optical densities**

559 A frozen culture of *S. oneidensis* was streaked onto an LB-agar plate then grown overnight at
560 30 ºC. A single colony was isolated and grown in LB media at 30 ºC under continuous shaking
561 (200 rpm). The optical density ($O.D._{600}$) of the culture was measured hourly using a Thermo
562 Fisher Scientific™ Nanodrop to observe the absorbance of the solution at a wavelength of 600
563 nm. When the culture reached exponential growth phase (at an $O.D._{600}$ of 0.5), the bacterial
564 culture was diluted to achieve variable $O.D._{600}$ values and was added to graphene oxide (0.12
565 g/L) in LB that had been flushed with nitrogen for 10 minutes to achieve anaerobic conditions.

566 **Generation of plate reader and image data**

567 At specific time points, the samples prepared above were placed in a light box to reduce
568 interference from changing lighting and background and imaged with a Google© Pixel phone.
569 RAW image files were used for analysis to avoid any interference from the imaging software.
570 RAW image files were converted to JPEG files using Adobe Lightroom© with no editing. The
571 JPEG images were used for image analysis in MATLAB©.

572 Immediately after imaging, 100 µL aliquots were taken from each sample. The aliquots were
573 placed into a 96 well plate, and their optical absorbance at 610 nm was measured using a
574 Biotek© Synergy H1 microplate reader. These concurrent measurements enabled direct
575 comparison between the measurements of graphene oxide reduction by digital image analysis
576 and plate reader absorbance measurements of the same samples.

577 **Color analysis of graphene oxide reduction sample images**

578 The JPEG images obtained of graphene oxide reduction samples were subjected to further
579 image analysis to obtain the average of the HSV value vector of each sample at different time-
580 points. A workflow of the analysis procedure is presented in Figure 1. Analysis code was

581 written in-house in MATLAB© and is available in the SI. For each image, the sample was
582 selected and cropped to select an area that had minimal interference from background or
583 reflections (Figure 1A). The orientation, location, focus, and selected area were kept consistent
584 between images within an experiment. Within the selected area, at least 12 points were selected,
585 avoiding any regions featuring reflections (Figure 1B). Around each point, a 32 x 32 pixel box
586 was generated. The color data was represented by the HSV color space, which contains the
587 color information of the selected crop box with three vectors[52] (Figure 1C). The H vector
588 contains hue information: the color of each pixel. The S vector contains saturation information:
589 how intense each pixel is. The V vector contains value information: how light or dark each
590 pixel is. The HSV color space is advantageous over other color spaces for image analysis, such
591 as the more typical RGB, because the data obtained is more stable under changing lighting
592 conditions[53]. The value vector was isolated, and the average value was taken over the entire
593 box. Each pixel was represented by a number between 0 and 1, where 0 is the darkest and 1 is
594 the lightest. This average value was calculated for each selected point, and the average overall
595 value across all the points was determined to obtain an average across each sample. This
596 method allowed for determination of the standard deviation over the sample for the analyzed
597 points.

598 **Image analysis of different graphene oxide concentrations**

599 To determine the correlation of the value vector with the concentration of graphene oxide,
600 different percentages of graphene oxide were mixed with LB media. Graphene oxide
601 percentages ranged from 0.1% - 100%. Images were taken of the different samples in a
602 lightbox, and the images were analysed digitally as described in the previous section. Average
603 HSV vectors of the samples were compared to observe whether higher concentrations of
604 graphene oxide corresponded to higher vector measurements.

605 **Analysis of graphene oxide reduction by *S. oneidensis* electroactivity-deficient strains**

606 Three identical 24-well tissue culture plates (Fisherbrand, Thermo-Fisher Scientific) were
607 prepared, each containing 3 replicate samples of *S. oneidensis* knockout strains
608 *ΔmtrDΔmtrCΔomcAΔmtrF, ΔomcAΔmtrC, ΔmtrCΔomcAΔmtrF*, or wild-type strain MR-1.
609 Each sample well contained 1 mL LB media with 5% (0.05 g) graphene oxide and was
610 inoculated with a 1:100 dilution of overnight bacteria culture. Samples were sealed with
611 optically clear tape (McMaster-Carr) to prevent evaporation and were incubated at 30ºC. Two
612 of these plates were analysed using image analysis, and one plate was analysed using the
613 Biotek© Synergy H1 microplate reader with measurements taken at 610 nm absorbance for 26
614 hours.

615 **Image analysis of graphene oxide reduction at different scales**

616 An overnight culture of MR-1 was inoculated at 1:100 dilution into LB media containing 5%
617 graphene oxide (1 g / L), using volumes of 1 mL, 10 mL, 40 mL, or 200 mL. The solutions
618 were incubated at 30 ºC in 24 well tissue culture plates (Fisherbrand, Thermo-Fisher
619 Scientific), 40 mL EPA vials (Sigma-Aldrich), 50 mL centrifuge tubes (Sigma-Aldrich), or 250
620 mL media bottles (Sigma-Aldrich) respectively. Imaging was performed using a Miroco SAD
621 lamp (Miroco) in a lightbox for even illumination. Error was calculated as the standard
622 deviation of three replicate samples.

623 **Application of the image analysis methodology by different users**

624 Six different users with no prior exposure to the image analysis methodology were asked to
625 select a region of an image that accurately represented the color of a 40 mL centrifuge tube
626 from the previous experiment at the 3.5-hour timepoint. Users were then asked to select ten
627 or more points from the section they had selected that accurately represented the color. No

other instruction was provided. The HSV value was then calculated for each selected point, and the median HSV value for each user's points was determined.

Statistical analysis of data trends

Analysis was performed using Graphpad Prism™ to obtain p-values. An ANOVA test was performed with a Welch's correction to obtain the statistical difference between different sample trends.

Bootstrapping analysis was performed following the methods of B. Efron & R. Tibshirani (1993)[58,95]. Let $x_1, \dots, x_n$ be a sample distribution from a distribution with mean $\bar{x}$ and variance σ_x^2. Let $y_1, \dots, y_n$ be an independent sample distribution with mean $\bar{y}$ and variance σ_y^2. Then the test statistic is calculated as:

$$t = \frac{\bar{x} - \bar{y}}{\sqrt{\left(\frac{\sigma_x^2}{n}\right) + \left(\frac{\sigma_y^2}{n}\right)}}$$

Then create two new data sets where the values are $x_i' = x_i - \bar{x} + \bar{z}$ and $y_i' = y_i - \bar{y} + \bar{z}$, where $\bar{z}$ is the mean of the combined sample. Draw a random sample (x_i^*) of size n points from this pooled sample with replacement from x_i'. Draw another random sample (y_i^*) of size m points from this pooled sample with replacement from y_i'. Then calculate the test statistic:

$$t^* = \frac{\overline{x^*} - \overline{y^*}}{\sqrt{\left(\frac{\sigma^{*2}_x}{n}\right) + \left(\frac{\sigma^{*2}_y}{m}\right)}}$$

Repeat this algorithm 1,000,000 times (B = 100000) to estimate the p-value as:

$$p = \frac{\sum_0^B I\{t^* \geq t\}}{B}$$

Where $I\{t^* \geq t\}$ =1 when the condition is true. This method is advantageous for estimating the p-value from smaller datasets[58].

ACKNOWLEDGEMENTS

The authors wish to thank Professor Todd Krauss and Professor Kara Bren for initial discussions concerning the spectroscopy of the graphene oxide flocculates. *Shewanella oneidensis* knockout strains were kindly gifted by Dr. Jeffrey Gralnick (University of Minnesota). The authors also wish to thank Dr. Elio Abbondanzieri for advice regarding bootstrapping analysis. The authors also wish to thank Linaria Larkin, Tiana Rohe, Jordan Kassanoff, Azra M. Walker, Dr. Elio A. Abbondanzieri, and Elliot Blues for their assistance in testing the consistency of the image analysis code. Funding to D.B. and A.S.M. was provided by the Department of Energy via DE-SC0023354.

REFERENCES

(1) Harris, H. W.; El-Naggar, M. Y.; Nealson, K. H. Shewanella Oneidensis MR-1 Chemotaxis Proteins and Electron-Transport Chain Components Essential for Congregation near Insoluble Electron Acceptors. *Biochem. Soc. Trans.* **2012**, *40* (6), 1167–1177. https://doi.org/10.1042/BST20120232.

(2) Edwards, E. H.; Jelusic, J.; Kosko, R. M.; McClelland, K. P.; Ngarnim, S. S.; Chiang, W.; Lampa-Pastirk, S.; Krauss, T. D.; Bren, K. L. Shewanella Oneidensis MR-1 Respires CdSe Quantum Dots for Photocatalytic Hydrogen Evolution. *PNAS* **2023**, *120*, 17. https://doi.org/10.1073/pnas.

(3) El-Naggar, M. Y.; Wanger, G.; Leung, K. M.; Yuzvinsky, T. D.; Southam, G.; Yang, J.; Lau, W. M.; Nealson, K. H.; Gorby, Y. A. Electrical Transport along Bacterial

Nanowires from Shewanella Oneidensis MR-1. *Proc. Natl. Acad. Sci. U. S. A.* **2010**, *107* (42), 18127–18131. https://doi.org/10.1073/pnas.1004880107.

(4) Rabaey, K.; Verstraete, W. Microbial Fuel Cells: Novel Biotechnology for Energy Generation. *Trends Biotechnol.* **2005**, *23* (6), 291–298. https://doi.org/10.1016/j.tibtech.2005.04.008.

(5) Rabaey, K.; Lissens, G.; Siciliano, S. D.; Verstraete, W. A Microbial Fuel Cell Capable of Converting Glucose to Electricity at High Rate and Efficiency. *Biotechnol. Lett.* **2003**, *25* (18), 1531–1535. https://doi.org/10.1023/A:1025484009367.

(6) Tao, M.; Jin, C.; Lu, H.; Jin, K.; Yu, L.; Liu, J.; Zhang, J.; Zhu, X.; Wu, Y. Living and Regenerative Material Encapsulating Self-Assembled Shewanella Oneidensis-CdS Hybrids for Photocatalytic Biodegradation of Organic Dyes. *Microorganisms* **2022**, *10* (12). https://doi.org/10.3390/microorganisms10122501.

(7) Cai, P. J.; Xiao, X.; He, Y. R.; Li, W. W.; Chu, J.; Wu, C.; He, M. X.; Zhang, Z.; Sheng, G. P.; Lam, M. H. W.; Xu, F.; Yu, H. Q. Anaerobic Biodecolorization Mechanism of Methyl Orange by Shewanella Oneidensis MR-1. *Appl. Microbiol. Biotechnol.* **2012**, *93* (4), 1769–1776. https://doi.org/10.1007/s00253-011-3508-8.

(8) Li, Q.; Feng, X.; Lu, X.; Li, T.; Han, X.; Xiao, X.; Wu, X.; Liu, Z.; Yang, M.; Feng, Y. Combined Intra- and Extracellular Reduction Involved in the Anaerobic Biodecolorization of Cationic Azo Dye by Shewanella Oneidensis MR-1. *Chemosphere* **2018**, *211*, 701–708. https://doi.org/10.1016/j.chemosphere.2018.08.006.

(9) Zhang, X.; Epifanio, M.; Marsili, E. Electrochemical Characteristics of Shewanella Loihica on Carbon Nanotubes-Modified Graphite Surfaces. *Electrochim. Acta* **2013**,

692 *102*, 252–258. https://doi.org/10.1016/j.electacta.2013.04.039.

693 (10) Gorby, Y. A.; Yanina, S.; McLean, J. S.; Rosso, K. M.; Moyles, D.; Dohnalkova, A.;
694 Beveridge, T. J.; Chang, I. S.; Kim, B. H.; Kim, K. S.; Culley, D. E.; Reed, S. B.;
695 Romine, M. F.; Saffarini, D. A.; Hill, E. A.; Shi, L.; Elias, D. A.; Kennedy, D. W.;
696 Pinchuk, G.; Watanabe, K.; Ishii, S.; Logan, B.; Nealson, K. H.; Fredrickson, J. K.
697 Electrically Conductive Bacterial Nanowires Produced by Shewanella Oneidensis
698 Strain MR-1 and Other Microorganisms. *Proc. Natl. Acad. Sci. U. S. A.* **2006**, *103*
699 (30), 11358–11363. https://doi.org/10.1073/pnas.0604517103.

700 (11) Lehner, B. A. E.; Janssen, V. A. E. C.; Spiesz, E. M.; Benz, D.; Brouns, S. J. J.;
701 Meyer, A. S.; van der Zant, H. S. J. Creation of Conductive Graphene Materials by
702 Bacterial Reduction Using Shewanella Oneidensis. *ChemistryOpen* **2019**, *8* (7), 888–
703 895. https://doi.org/10.1002/open.201900186.

704 (12) Ford, K. C.; TerAvest, M. A. The Electron Transport Chain of Shewanella Oneidensis
705 MR-1 Can Operate Bidirectionally to Enable Microbial Electrosynthesis. *Appl.*
706 *Environ. Microbiol.* **2024**, *90* (1). https://doi.org/10.1128/aem.01387-23.

707 (13) Liu, W.; Liu, L.; Liu, C.; Hao, Y.; Yang, H.; Yuan, B.; Jiang, J. Methylene Blue
708 Enhances the Anaerobic Decolorization and Detoxication of Azo Dye by Shewanella
709 Onediensis MR-1. *Biochem. Eng. J.* **2016**, *110*, 115–124.
710 https://doi.org/10.1016/j.bej.2016.02.012.

711 (14) Torres, C. I.; Krajmalnik-Brown, R.; Parameswaran, P.; Marcus, A. K.; Wanger, G.;
712 Gorby, Y. A.; Rittmann, B. E. Selecting Anode-Respiring Bacteria Based on Anode
713 Potential: Phylogenetic, Electrochemical, and Microscopic Characterization. *Environ.*
714 *Sci. Technol.* **2009**, *43* (24), 9519–9524. https://doi.org/10.1021/es902165y.

715 (15) Jiao, Y.; Qian, F.; Li, Y.; Wang, G.; Saltikov, C. W.; Gralnick, J. A. Deciphering the
716 Electron Transport Pathway for Graphene Oxide Reduction by Shewanella Oneidensis
717 MR-1. *J. Bacteriol.* **2011**, *193* (14), 3662–3665. https://doi.org/10.1128/JB.00201-11.

718 (16) Kotloski, N. J.; Gralnick, J. A. Flavin Electron Shuttles Dominate Extracellular
719 Electron Transfer by Shewanella Oneidensis. **2013**, *4* (1), 10–13.
720 https://doi.org/10.1128/mBio.00553-12.Editor.

721 (17) Pirbadian, S.; Barchinger, S. E.; Leung, K. M.; Byun, H. S.; Jangir, Y.; Bouhenni, R.
722 A.; Reed, S. B.; Romine, M. F.; Saffarini, D. A.; Shi, L.; Gorby, Y. A.; Golbeck, J. H.;
723 El-Naggar, M. Y. Shewanella Oneidensis MR-1 Nanowires Are Outer Membrane and
724 Periplasmic Extensions of the Extracellular Electron Transport Components. *Proc.*
725 *Natl. Acad. Sci. U. S. A.* **2014**, *111* (35), 12883–12888.
726 https://doi.org/10.1073/pnas.1410551111.

727 (18) Subramanian, P.; Pirbadian, S.; El-Naggar, M. Y.; Jensen, G. J. Ultrastructure of
728 Shewanella Oneidensis MR-1 Nanowires Revealed by Electron Cryotomography.
729 *Proc. Natl. Acad. Sci. U. S. A.* **2018**, *115* (14), E3246–E3255.
730 https://doi.org/10.1073/pnas.1718810115.

731 (19) Harris, H. W.; Sánchez-Andrea, I.; McLean, J. S.; Salas, E. C.; Tran, W.; El-Naggar,
732 M. Y.; Nealson, K. H. Redox Sensing within the Genus Shewanella. *Front. Microbiol.*
733 **2018**, *8* (JAN), 1–11. https://doi.org/10.3389/fmicb.2017.02568.

734 (20) Beliaev, A. S.; Saffarini, D. A.; McLaughlin, J. L.; Hunnicutt, D. MtrC, an Outer
735 Membrane Decahaem c Cytochrome Required for Metal Reduction in Shewanella
736 Putrefaciens MR-1. *Mol. Microbiol.* **2001**, *39* (3), 722–730.
737 https://doi.org/10.1046/j.1365-2958.2001.02257.x.

738 (21) Wu, C.; Cheng, Y. Y.; Li, B. B.; Li, W. W.; Li, D. B.; Yu, H. Q. Electron Acceptor
739 Dependence of Electron Shuttle Secretion and Extracellular Electron Transfer by
740 Shewanella Oneidensis MR-1. *Bioresour. Technol.* **2013**, *136*, 711–714.
741 https://doi.org/10.1016/j.biortech.2013.02.072.

742 (22) Dong, Z.; Guo, S.; Fu, H.; Gao, H. Investigation of a Spontaneous Mutant Reveals
743 Novel Features of Iron Uptake in Shewanella Oneidensis. *Sci. Rep.* **2017**, *7* (1), 1–12.
744 https://doi.org/10.1038/s41598-017-11987-3.

745 (23) Wang, G.; Qian, F.; Saltikov, C. W.; Jiao, Y.; Li, Y. Microbial Reduction of Graphene
746 Oxide by Shewanella. *Nano Res.* **2011**, *4* (6), 563–570.
747 https://doi.org/10.1007/s12274-011-0112-2.

748 (24) Shi, L.; Squier, T. C.; Zachara, J. M.; Fredrickson, J. K. Respiration of Metal
749 (Hydr)Oxides by Shewanella and Geobacter: A Key Role for Multihaem c-Type
750 Cytochromes. *Mol. Microbiol.* **2007**, *65* (1), 12–20. https://doi.org/10.1111/j.1365-
751 2958.2007.05783.x.

752 (25) McLean, J. S.; Pinchuk, G. E.; Geydebrekht, O. V.; Bilskis, C. L.; Zakrajsek, B. A.;
753 Hill, E. A.; Saffarini, D. A.; Romine, M. F.; Gorby, Y. A.; Fredrickson, J. K.; Beliaev,
754 A. S. Oxygen-Dependent Autoaggregation in Shewanella Oneidensis MR-1. *Environ.*
755 *Microbiol.* **2008**, *10* (7), 1861–1876. https://doi.org/10.1111/j.1462-
756 2920.2008.01608.x.

757 (26) Brown, S. D.; Thompson, M. R.; VerBerkmoes, N. C.; Chourey, K.; Shah, M.; Zhou,
758 J.; Hettich, R. L.; Thompson, D. K. Molecular Dynamics of the Shewanella Oneidensis
759 Response to Chromate Stress. *Mol. Cell. Proteomics* **2006**, *5* (6), 1054–1071.
760 https://doi.org/10.1074/mcp.M500394-MCP200.

761 (27) Breuer, M.; Rosso, K. M.; Blumberger, J.; Butt, J. N. Multi-Haem Cytochromes in
762 Shewanella Oneidensis MR-1: Structures, Functions and Opportunities. *J. R. Soc.*
763 *Interface* **2015**, *12* (102). https://doi.org/10.1098/rsif.2014.1117.

764 (28) Boas, J. V.; Oliveira, V. B.; Simões, M.; Pinto, A. M. F. R. Review on Microbial Fuel
765 Cells Applications, Developments and Costs. *J. Environ. Manage.* **2022**, *307* (April
766 2021). https://doi.org/10.1016/j.jenvman.2022.114525.

767 (29) Logan, B. E.; Regan, J. M. Microbial Fuel Cells - Challenges and Applications. *Fuel*
768 *Cells Technol. Fuel Process.* **2006**, No. 10, 1–32.

769 (30) Wang, H.; Correa, E.; Dunn, W. B.; Winder, C. L.; Goodacre, R.; Lloyd, J. R.
770 Metabolomic Analyses Show That Electron Donor and Acceptor Ratios Control
771 Anaerobic Electron Transfer Pathways in Shewanella Oneidensis. *Metabolomics* **2013**,
772 *9* (3), 642–656. https://doi.org/10.1007/s11306-012-0488-3.

773 (31) Starwalt-Lee, R.; El-Naggar, M. Y.; Bond, D. R.; Gralnick, J. A. Electrolocation? The
774 Evidence for Redox-Mediated Taxis in Shewanella Oneidensis. *Mol. Microbiol.* **2021**,
775 *115* (6), 1069–1079. https://doi.org/10.1111/mmi.14647.

776 (32) Ntarlagiannis, D.; Atekwana, E. A.; Hill, E. A.; Gorby, Y. Microbial Nanowires: Is the
777 Subsurface "Hardwired"? *Geophys. Res. Lett.* **2007**, *34* (17), 3–7.
778 https://doi.org/10.1029/2007GL030426.

779 (33) Coursolle, D.; Baron, D. B.; Bond, D. R.; Gralnick, J. A. The Mtr Respiratory Pathway
780 Is Essential for Reducing Flavins and Electrodes in Shewanella Oneidensis. *J.*
781 *Bacteriol.* **2010**, *192* (2), 467–474. https://doi.org/10.1128/JB.00925-09.

782 (34) Jin, X.; Wu, Y.; Peacock, C. L. .; Ashry, N. M.; Gao, C.; Huang, Q.; Cai, P. Outer
783 Membrane C-Type Cytochromes OmcA and MtrC Play Distinct Roles in Enhancing

784 the Attachment of Shewanella Oneidensis MR-1 Cells to Goethite. *Environ. Microbiol.*
785 **2020**, *86* (23), 1–17.

786 (35) Roy, J. N.; Garcia, K. E.; Luckarift, H. R.; Falase, A.; Cornejo, J.; Babanova, S.;
787 Schuler, A. J.; Johnson, G. R.; Atanassov, P. B. Applied Electrode Potential Leads to
788 Shewanella Oneidensis MR-1 Biofilms Engaged in Direct Electron Transfer . *J.*
789 *Electrochem. Soc.* **2013**, *160* (11), H866–H871. https://doi.org/10.1149/2.001401jes.

790 (36) Beliaev, A. S.; Klingeman, D. M.; Klappenbach, J. A.; Wu, L.; Romine, M. F.; Tiedje,
791 J. M.; Nealson, K. H.; Fredrickson, J. K.; Zhou, J. Global Transcriptome Analysis of
792 Shewanella Oneidensis MR-1 Exposed to Different Terminal Electron Acceptors. *J.*
793 *Bacteriol.* **2005**, *187* (20), 7138–7145. https://doi.org/10.1128/JB.187.20.7138-
794 7145.2005.

795 (37) Hong, Y.; Chen, X.; Guo, J.; Xu, Z.; Xu, M.; Sun, G. Effects of Electron Donors and
796 Acceptors on Anaerobic Reduction of Azo Dyes by Shewanella Decolorationis S12.
797 *Appl. Microbiol. Biotechnol.* **2007**, *74* (1), 230–238. https://doi.org/10.1007/s00253-
798 006-0657-2.

799 (38) Voeikova, T. A.; Emel'yanova, L. K.; Novikova, L. M.; Mordkovich, N. N.; Shakulov,
800 R. S.; Debabov, V. G. Mutants of an Electrogenic Bacterium Shewanella Oneidensis
801 MR-1 with Increased Reducing Activity. *Microbiol. (Russian Fed.* **2012**, *81* (3), 312–
802 316. https://doi.org/10.1134/S0026261712030162.

803 (39) Bennett, B. D.; Brutinel, E. D.; Gralnick, J. A. A Ferrous Iron Exporter Mediates Iron
804 Resistance in Shewanella Oneidensis MR-1. *Appl. Environ. Microbiol.* **2015**, *81* (22),
805 7938–7944. https://doi.org/10.1128/AEM.02835-15.

806 (40) Graham, A. J.; Gibbs, S. L.; Saez Cabezas, C. A.; Wang, Y.; Green, A. M.; Milliron,

807 D. J.; Keitz, B. K. In Situ Optical Quantification of Extracellular Electron Transfer
808 Using Plasmonic Metal Oxide Nanocrystals**. *ChemElectroChem* **2022**, *9* (3).
809 https://doi.org/10.1002/celc.202101423.

810 (41) Chang, L. Y.; Li, Y. Y.; Li, C. T.; Lee, C. P.; Fan, M. S.; Vittal, R.; Ho, K. C.; Lin, J.
811 J. A Composite Catalytic Film of Ni-NPs/PEDOT: PSS for the Counter Electrodes in
812 Dye-Sensitized Solar Cells. *Electrochim. Acta* **2014**, *146*, 697–705.
813 https://doi.org/10.1016/j.electacta.2014.08.112.

814 (42) Lamberg, P.; Bren, K. L. Extracellular Electron Transfer on Sticky Paper Electrodes:
815 Carbon Paste Paper Anode for Microbial Fuel Cells. *ACS Energy Lett.* **2016**, *1* (5),
816 895–898. https://doi.org/10.1021/acsenergylett.6b00435.

817 (43) Baron, D.; LaBelle, E.; Coursolle, D.; Gralnick, J. A.; Bond, D. R. Electrochemical
818 Measurement of Electron Transfer Kinetics by Shewanella Oneidensis MR-1. *J. Biol.*
819 *Chem.* **2009**, *284* (42), 28865–28873. https://doi.org/10.1074/jbc.M109.043455.

820 (44) Park, D.; Zeikus, J. Impact of Electrode Composition on Electricity Generation in a
821 Single-Compartment Fuel Cell Using Shewanella Putrefaciens. *Appl. Microbiol.*
822 *Biotechnol.* **2002**, *59* (1), 58–61. https://doi.org/10.1007/s00253-002-0972-1.

823 (45) Esmaeili, Y.; Bidram, E.; Zarrabi, A.; Amini, A.; Cheng, C. Graphene Oxide and Its
824 Derivatives as Promising In-Vitro Bio-Imaging Platforms. **1993**, *10* (1), 1–13.

825 (46) Shih, C. J.; Lin, S.; Sharma, R.; Strano, M. S.; Blankschtein, D. Understanding the PH-
826 Dependent Behavior of Graphene Oxide Aqueous Solutions: A Comparative
827 Experimental and Molecular Dynamics Simulation Study. *Langmuir* **2012**, *28* (1),
828 235–241. https://doi.org/10.1021/la203607w.

829 (47) Gao, Y.; Zeng, X.; Zhang, W.; Zhou, L.; Xue, W.; Tang, M.; Sun, S. The Aggregation

Behaviour and Mechanism of Commercial Graphene Oxide in Surface Aquatic Environments. *Sci. Total Environ.* **2022**, *806*, 150942. https://doi.org/10.1016/j.scitotenv.2021.150942.

(48) Fennessey, C. M.; Jones, M. E.; Taillefert, M.; Dichristina, T. J. Siderophores Are Not Involved in Fe(III) Solubilization during Anaerobic Fe(III) Respiration by Shewanella Oneidensis MR-1. *Appl. Environ. Microbiol.* **2010**, *76* (8), 2425–2432. https://doi.org/10.1128/AEM.03066-09.

(49) Huang, N. M.; Lim, H. N.; Chia, C. H.; Yarmo, M. A.; Muhamad, M. R. Simple Room-Temperature Preparation of High-Yield Large-Area Graphene Oxide. *Int. J. Nanomedicine* **2011**, *6*, 3443–3448. https://doi.org/10.2147/ijn.s26812.

(50) Cheng, X.; Dai, D.; Yuan, Z.; Peng, L.; He, Y.; Yeung, E. S. Color Difference Amplification between Gold Nanoparticles in Colorimetric Analysis with Actively Controlled Multiband Illumination. *Anal. Chem.* **2014**, *86* (15), 7584–7592. https://doi.org/10.1021/ac501448w.

(51) Ouyang, M.; Di Carlo, D. Nanoplasmonic Swarm Biosensing Using Single Nanoparticle Colorimetry. *Biosens. Bioelectron.* **2019**, *132* (January), 162–170. https://doi.org/10.1016/j.bios.2019.02.056.

(52) Liu, Z.; Chen, W.; Zou, Y.; Hu, C. Regions of Interest Extraction Based on HSV Color Space. *IEEE Int. Conf. Ind. Informatics* **2012**, 481–485. https://doi.org/10.1109/INDIN.2012.6301214.

(53) Bennett, D.; Chen, X.; Walker, G. J.; Stelzer-Braid, S.; Rawlinson, W. D.; Hibbert, D. B.; Tilley, R. D.; Gooding, J. J. Machine Learning Color Feature Analysis of a High Throughput Nanoparticle Conjugate Sensing Assay. *Anal. Chem.* **2023**, *95* (16), 6550–

6558. https://doi.org/10.1021/acs.analchem.2c05292.

(54) Bora, D. J.; Gupta, A. K.; Khan, F. A. Comparing the Performance of L*A*B* and HSV Color Spaces with Respect to Color Image Segmentation. *Int. J. Emerg. Technol. Adv. Eng.* **2015**, *5* (2), 192–203.

(55) Howell, D.; Rogier, M.; Yzerbyt, V.; Bestgen, Y. Statistical Methods in Human Sciences. *New York Wadsworth* **1998**.

(56) Hibbert, D. B.; Gooding, J. J. *Data Analysis for Chemistry*; Oxford University Press, 2005. https://doi.org/10.1093/oso/9780195162103.001.0001.

(57) Delacre, M.; Leys, C.; Mora, Y. L.; Lakens, D. Taking Parametric Assumptions Seriously: Arguments for the Use of Welch's f-Test Instead of the Classical f-Test in One-Way ANOVA. *Int. Rev. Soc. Psychol.* **2020**, *32* (1), 1–12. https://doi.org/10.5334/IRSP.198.

(58) Efron, B.; Tibshirani, R. *An Introduction to the Bootstrap*; Chapman & Hall, 1993; Vol. 23. https://doi.org/10.1111/1467-9639.00050.

(59) Wang, J.; Guo, X. The Gompertz Model and Its Applications in Microbial Growth and Bioproduction Kinetics: Past, Present and Future. *Biotechnol. Adv.* **2024**, *72* (February), 108335. https://doi.org/10.1016/j.biotechadv.2024.108335.

(60) Tjørve, K. M. C.; Tjørve, E. The Use of Gompertz Models in Growth Analyses, and New Gompertz-Model Approach: An Addition to the Unified-Richards Family. *PLoS One* **2017**, *12* (6), 1–17. https://doi.org/10.1371/journal.pone.0178691.

(61) Zwietering, M. H.; Jongenburger, I.; Rombouts, F. M.; Van't Riet, K. Modeling of the Bacterial Growth Curve. *Appl. Environ. Microbiol.* **1990**, *56* (6), 1875–1881.

875 https://doi.org/10.1128/aem.56.6.1875-1881.1990.

876 (62) Alupoaei, C. E.; García-Rubio, L. H. Growth Behavior of Microorganisms Using UV-
877 Vis Spectroscopy: Escherichia Coli. *Biotechnol. Bioeng.* **2004**, *86* (2), 163–167.
878 https://doi.org/10.1002/bit.20001.

879 (63) Emiru, T. F.; Ayele, D. W. Controlled Synthesis, Characterization and Reduction of
880 Graphene Oxide: A Convenient Method for Large Scale Production. *Egypt. J. Basic*
881 *Appl. Sci.* **2017**, *4* (1), 74–79. https://doi.org/10.1016/j.ejbas.2016.11.002.

882 (64) Bencheikh-Latmani, R.; Williams, S. M.; Haucke, L.; Criddle, C. S.; Wu, L.; Zhou, J.;
883 Tebo, B. M. Global Transcriptional Profiling of Shewanella Oneidensis MR-1 during
884 Cr(VI) and U(VI) Reduction. *Appl. Environ. Microbiol.* **2005**, *71* (11), 7453–7460.
885 https://doi.org/10.1128/AEM.71.11.7453-7460.2005.

886 (65) Myers, C. R.; Myers, J. M. MtrB Is Required for Proper Incorporation of the
887 Cytochromes OmcA and OmcB into the Outer Membrane of Shewanella Putrefaciens
888 MR-1. *Appl. Environ. Microbiol.* **2002**, *68* (11), 5585–5594.
889 https://doi.org/10.1128/AEM.68.11.5585-5594.2002.

890 (66) Smida, H.; Langlard, A.; Thomas, L.; Thobie-Gautier, C.; Boujtita, M.; Louro, R. O.;
891 Paquete, C. M.; Lebègue, E. Exploring the Effect of Shewanella Oneidensis Outer
892 Membrane Redox Proteins in the Electrochemical Response of Single Blocking Impact
893 Events. *Electrochim. Acta* **2024**, *488* (March), 6–11.
894 https://doi.org/10.1016/j.electacta.2024.144235.

895 (67) Thompson, D. K.; Beliaev, A. S.; Giometti, C. S.; Tollaksen, S. L.; Khare, T.; Lies, D.
896 P.; Nealson, K. H.; Lim, H.; Yates, J.; Brandt, C. C.; Tiedje, J. M.; Zhou, J.
897 Transcriptional and Proteomic Analysis of a Ferric Uptake Regulator (Fur) Mutant of

Shewanella Oneidensis: Possible Involvement of Fur in Energy Metabolism, Transcriptional Regulation, and Oxidative Stress. *Appl. Environ. Microbiol.* **2002**, *68* (2), 881–892. https://doi.org/10.1128/AEM.68.2.881-892.2002.

(68) Gabrielson, J.; Hart, M.; Jarelöv, A.; Kühn, I.; McKenzie, D.; Möllby, R. Evaluation of Redox Indicators and the Use of Digital Scanners and Spectrophotometer for Quantification of Microbial Growth in Microplates. *J. Microbiol. Methods* **2002**, *50* (1), 63–73. https://doi.org/10.1016/S0167-7012(02)00011-8.

(69) Uno, M.; Phansroy, N.; Aso, Y.; Ohara, H. Starch-Fueled Microbial Fuel Cells by Two-Step and Parallel Fermentation Using Shewanella Oneidensis MR-1 and Streptococcus Bovis 148. *J. Biosci. Bioeng.* **2017**, *124* (2), 189–194. https://doi.org/10.1016/j.jbiosc.2017.03.016.

(70) Pinchuk, G. E.; Geydebrekht, O. V.; Hill, E. A.; Reed, J. L.; Konopka, A. E.; Beliaev, A. S.; Fredrickson, J. K. Pyruvate and Lactate Metabolism by Shewanella Oneidensis MR-1 under Fermentation, Oxygen Limitation, and Fumarate Respiration Conditions. *Appl. Environ. Microbiol.* **2011**, *77* (23), 8234–8240. https://doi.org/10.1128/AEM.05382-11.

(71) Fitzgerald, L. A.; Petersen, E. R.; Gross, B. J.; Soto, C. M.; Ringeisen, B. R.; El-Naggar, M. Y.; Biffinger, J. C. Aggrandizing Power Output from Shewanella Oneidensis MR-1 Microbial Fuel Cells Using Calcium Chloride. *Biosens. Bioelectron.* **2012**, *31* (1), 492–498. https://doi.org/10.1016/j.bios.2011.11.024.

(72) Torres, C. I.; Marcus, A. K.; Rittmann, B. E. Proton Transport inside the Biofilm Limits Electrical Current Generation by Anode-Respiring Bacteria. *Biotechnol. Bioeng.* **2008**, *100* (5), 872–881. https://doi.org/10.1002/bit.21821.

921 (73) McCoy, T. M.; Pottage, M. J.; Tabor, R. F. Graphene Oxide-Stabilized Oil-in-Water
922 Emulsions: PH-Controlled Dispersion and Flocculation. *J. Phys. Chem. C* **2014**, *118*
923 (8), 4529–4535. https://doi.org/10.1021/jp500072a.

924 (74) Nanda, S. S.; Yi, D. K.; Kim, K. Study of Antibacterial Mechanism of Graphene Oxide
925 Using Raman Spectroscopy. *Sci. Rep.* **2016**, *6* (March), 1–12.
926 https://doi.org/10.1038/srep28443.

927 (75) Gurunathan, S.; Han, J. W.; Abdal Dayem, A.; Eppakayala, V.; Kim, J. H. Oxidative
928 Stress-Mediated Antibacterial Activity of Graphene Oxide and Reduced Graphene
929 Oxide in Pseudomonas Aeruginosa. *Int. J. Nanomedicine* **2012**, *7*, 5901–5914.
930 https://doi.org/10.2147/IJN.S37397.

931 (76) Elias, D. A.; Tollaksen, S. L.; Kennedy, D. W.; Mottaz, H. M.; Giometti, C. S.;
932 McLean, J. S.; Hill, E. A.; Pinchuk, G. E.; Lipton, M. S.; Fredrickson, J. K.; Gorby, Y.
933 A. The Influence of Cultivation Methods on Shewanella Oneidensis Physiology and
934 Proteome Expression. *Arch. Microbiol.* **2008**, *189* (4), 313–324.
935 https://doi.org/10.1007/s00203-007-0321-y.

936 (77) Takeuchi, R.; Sugimoto, Y.; Kitazumi, Y.; Shirai, O.; Ogawa, J.; Kano, K.
937 Electrochemical Study on the Extracellular Electron Transfer Pathway from
938 Shewanella Strain Hac319 to Electrodes. *Anal. Sci.* **2018**, *34* (10), 1177–1182.
939 https://doi.org/10.2116/analsci.18P237.

940 (78) Wenzel, T.; Härtter, D.; Bombelli, P.; Howe, C. J.; Steiner, U. Porous Translucent
941 Electrodes Enhance Current Generation from Photosynthetic Biofilms. *Nat. Commun.*
942 **2018**, *9* (1), 1–9. https://doi.org/10.1038/s41467-018-03320-x.

943 (79) Yuan, S. J.; Li, W. W.; Cheng, Y. Y.; He, H.; Chen, J. J.; Tong, Z. H.; Lin, Z. Q.;

944 Zhang, F.; Sheng, G. P.; Yu, H. Q. A Plate-Based Electrochromic Approach for the
945 High-Throughput Detection of Electrochemically Active Bacteria. *Nat. Protoc.* **2014**,
946 *9* (1), 112–119. https://doi.org/10.1038/nprot.2013.173.

947 (80) Lies, D. P.; Hernandez, M. E.; Kappler, A.; Mielke, R. E.; Gralnick, J. A.; Newman,
948 D. K. Shewanella Oneidensis MR-1 Uses Overlapping Pathways for Iron Reduction at
949 a Distance and by Direct Contact under Conditions Relevant for Biofilms. *Appl.*
950 *Environ. Microbiol.* **2005**, *71* (8), 4414–4426. https://doi.org/10.1128/AEM.71.8.4414-
951 4426.2005.

952 (81) Mclean, J. S.; Wanger, G.; Gorby, Y. A.; Wainstein, M.; Mcquaid, J.; Ishii, S. I.;
953 Bretschger, O.; Beyenal, H.; Nealson, K. H. Quantification of Electron Transfer Rates
954 to a Solid Phase Electron Acceptor through the Stages of Biofilm Formation from
955 Single Cells to Multicellular Communities. *Environ. Sci. Technol.* **2010**, *44* (7), 2721–
956 2727. https://doi.org/10.1021/es903043p.

957 (82) Lu, M.; Chan, S.; Babanova, S.; Bretschger, O. Effect of Oxygen on the Per-cell
958 Extracellular Electron Transfer Rate of Shewanella Oneidensis MR-1 Explored in
959 Bioelectrochemical Systems. *Biotechnol. Bioeng.* **2017**, *114* (1), 96–105.
960 https://doi.org/10.1002/bit.26046.

961 (83) Cao, Y.; Li, X.; Li, F.; Song, H. CRISPRi-SRNA: Transcriptional-Translational
962 Regulation of Extracellular Electron Transfer in Shewanella Oneidensis. *ACS Synth.*
963 *Biol.* **2017**, *6* (9), 1679–1690. https://doi.org/10.1021/acssynbio.6b00374.

964 (84) Ong, W. K.; Vu, T. T.; Lovendahl, K. N.; Llull, J. M.; Serres, M. H.; Romine, M. F.;
965 Reed, J. L. Comparisons of Shewanella Strains Based on Genome Annotations,
966 Modeling, and Experiments. *BMC Syst. Biol.* **2014**, *8* (1), 1–11.

https://doi.org/10.1186/1752-0509-8-31.

(85) Kitcha, S.; Cheirsilp, B. Enhanced Lipid Production by Co-Cultivation and Co-Encapsulation of Oleaginous Yeast Trichosporonoides Spathulata with Microalgae in Alginate Gel Beads. *Appl. Biochem. Biotechnol.* **2014**, *173* (2), 522–534. https://doi.org/10.1007/s12010-014-0859-5.

(86) Kregiel, D. Advances in Biofilm Control for Food and Beverage Industry Using Organo-Silane Technology: A Review. *Food Control* **2014**, *40* (1), 32–40. https://doi.org/10.1016/j.foodcont.2013.11.014.

(87) West, E. A.; Jain, A.; Gralnick, J. A. Engineering a Native Inducible Expression System in Shewanella Oneidensis to Control Extracellular Electron Transfer. *ACS Synth. Biol.* **2017**, *6* (9), 1627–1634. https://doi.org/10.1021/acssynbio.6b00349.

(88) Boyaval, P.; Corre, C.; Terre, S. Continuous Lactic Acid Fermentation with Concentrated Product Recovery by Ultrafiltration and Electrodialysis. *Biotechnol. Lett.* **1987**, *9* (3), 207–212. https://doi.org/10.1007/BF01024568.

(89) Tian, Z.; Xu, Y.; Lin, L. Multi-Scale Phenomena in Heterogeneous Catalytic Processes-Impact of Chemical Phenomena under the Micro-Scale Level on Catalyst Development and Design. *Chem. Eng. Sci.* **2004**, *59* (8–9), 1745–1753. https://doi.org/10.1016/j.ces.2004.01.030.

(90) Mitchell, S.; Michels, N. L.; Pérez-Ramírez, J. From Powder to Technical Body: The Undervalued Science of Catalyst Scale Up. *Chem. Soc. Rev.* **2013**, *42* (14), 6094–6112. https://doi.org/10.1039/c3cs60076a.

(91) Crater, J. S.; Lievense, J. C. Scale-up of Industrial Microbial Processes. *FEMS Microbiol. Lett.* **2018**, *365* (13), 1–5. https://doi.org/10.1093/femsle/fny138.

(92) Takors, R. Scale-up of Microbial Processes: Impacts, Tools and Open Questions. *J. Biotechnol.* **2012**, *160* (1–2), 3–9. https://doi.org/10.1016/j.jbiotec.2011.12.010.

(93) Coursolle, D.; Gralnick, J. A. Modularity of the Mtr Respiratory Pathway of Shewanella Oneidensis Strain MR-1. *Mol. Microbiol.* **2010**, *77* (4), 995–1008. https://doi.org/10.1111/j.1365-2958.2010.07266.x.

(94) Edwards, E. H. .; Jelusic, J.; Kosko, R. M. .; McClelland, K. P. .; Ngarnim, S. S. .; Chiang, W.; Lampa-Pastirk, S.; Krauss, T. D. .; Bren, K. L. Supplementary Information for Shewanella Oneidensis MR-1 Respire CdSe Quantum Dots for Photocatalytic. *PNAS* **2023**, *120* (17), 1–30. https://doi.org/https://doi.org/10.1073/pnas.2206975120.

(95) Efron, B. Second Thoughts on the Bootstrap. *Stat. Sci.* **2003**, *18* (2), 135–140. https://doi.org/10.1214/ss/1063994968.